processes

MDPI

*Article*

# $Cu_2O$-Electrodeposited $TiO_2$ Photoelectrode for Integrated Solar Redox Flow Battery

**Zihan Zhang [1], Ping Lu [1], Zixing Gu [1], Qiang Ma [1], Zhizhong Guo [2], Huaneng Su [1] and Qian Xu [1,*]**

[1] Institute for Energy Research, Jiangsu University, Zhenjiang 212013, China; zzh991218@outlook.com (Z.Z.); flightinglp@163.com (P.L.); guzixing991016@163.com (Z.G.); maqiang@ujs.edu.cn (Q.M.); suhuaneng@ujs.edu.cn (H.S.)

[2] College of Electrical and Mechanical Engineering, Hainan University, Haikou 570228, China; 990527@hainanu.edu.cn

* Correspondence: xuqian@ujs.edu.cn

**Abstract:** $TiO_2$ photoelectrode has become an attractive platform due to its excellent photoelectric performance and has been widely used in battery, photocatalysis, and other photoelectric fields. However, when the $TiO_2$ photoelectrode is used in solar flow batteries, the small photo-charging current is a potential problem, which will extend the charging process and lower the battery utilization efficiency. To address this issue, $Cu_2O$ is introduced to the surface of the $TiO_2$ photoelectrode, and $Cu_2O$-$TiO_2$ forms a heterojunction to improve battery performance in this work. The formation mechanism of $Cu_2O$-$TiO_2$ is revealed and utilized to deposit $Cu_2O$ on pre-treated FTO glass covered with $TiO_2$ films using electrochemical deposition (ECD). The photoelectrochemical properties of $Cu_2O$-$TiO_2$ photoelectrodes are characterized using XRD, UV-vis diffuse reflectance spectroscopy, XPS, and electrochemical characterizations. The successful deposition of $Cu_2O$ on the surface of $TiO_2$ photoelectrode is confirmed, and the UV-vis spectroscopic test results show that the incorporation of $Cu_2O$ enhances and broadens the absorption and utilization of sunlight in the UV range by the $TiO_2$ photoelectrode. Furthermore, the electrochemical test results manifest that the $Cu_2O$-$TiO_2$ photoelectrode possesses a higher carrier concentration under illumination conditions due to the formation of a heterojunction. Finally, a 30 min unbiased photocharging test demonstrates that the $Cu_2O$-$TiO_2$ photoelectrode charges in a current density of 425.03 $\mu A \cdot cm^{-2}$, indicating an increased photogenerated carrier concentration and a decreased photogenerated carrier recombination rate, which results from the enlarged doping concentration and improved charge transfer process at the electrolyte/semiconductor interface due to the incorporation of $Cu_2O$. Compared with the current density of 116.21 $\mu A \cdot cm^{-2}$ for the bare $TiO_2$ photoelectrode, the performance can be improved by over 365%.

**Keywords:** $TiO_2$; $Cu_2O$; photoelectrode; electrodeposition; integrated solar redox flow battery



**Citation:** Zhang, Z.; Lu, P.; Gu, Z.; Ma, Q.; Guo, Z.; Su, H.; Xu, Q. $Cu_2O$-Electrodeposited $TiO_2$ Photoelectrode for Integrated Solar Redox Flow Battery. *Processes* **2023**, *11*, 2631. https://doi.org/10.3390/pr11092631

Academic Editor: Zois Syrgiannis

Received: 11 August 2023
Revised: 28 August 2023
Accepted: 1 September 2023
Published: 3 September 2023



## 1. Introduction

Currently, due to the emergence of problems such as resource shortages and environmental pollution, people are beginning to pay more and more attention to clean energy sources such as solar and wind power. As one of the solutions to future energy needs, solar energy is expected to replace fossil energy sources while maintaining the current standard of living due to its nearly unlimited energy reserves. However, due to the intermittent nature of solar energy, the use of solar energy needs to be accompanied by the construction of appropriate energy storage facilities. The emergence of redox flow batteries (RFBs) provides new ideas for the construction of energy storage facilities. Due to their adjustable capacity and power design, RFBs are very suitable for large-scale energy storage. Therefore, solar energy and redox flow batteries are combined to form solar redox flow battery, and redox flow batteries are used as energy storage devices to overcome the shortcomings

of strong solar intermittency. However, the traditional solar redox flow battery is a split design, i.e., there are two separate systems for solar power generation and redox flow battery energy storage. Its energy conversion process is divided into three steps: solar energy, electrical energy, and chemical energy. Therefore, the traditional solar flow battery needs to be supported by the construction of solar-power-generation-related equipment, such as a maximum power point tracker and DC-DC converter. This undoubtedly increases the cost of system construction and reduces the reliability of the whole system. To address these shortcomings, a one-piece solar liquid flow battery configuration has been proposed [1–7], and the mechanism and design methodology of solar liquid flow batteries have been systematically investigated [8–10]. The Integrated solar flow battery has the advantage of in situ storage over the traditional configuration, i.e., the solar energy is directly converted into chemical energy for storage without the need of conversion into electrical energy in the middle. At the same time, the integrated design reduces many non-essential components, such as maximum power point tracking devices, which reduces the construction and utilization costs.

Among the many components of an integrated solar flow cell, the photoelectrode becomes the core component, and its proper selection can effectively enhance the performance of the cell. Among many photoelectrodes, oxide-based photoelectrodes [11] stand out due to their high abundance, low manufacturing cost, and excellent stability, and they have attracted much attention in various fields of photoelectrochemistry, such as the field of solar–hydrogen energy conversion [12–14], the field of lithium batteries [15], and the field of solar water splitting [16,17]. Among the many oxide-based photoelectrodes, the performance of $Cu_2O$ photoelectrodes is comparable to that of many photovoltaic semiconductor-based photoelectrodes [18]. For this reason, the mechanism of heterojunction formation in $Cu_2O$ photoelectrodes [19] has been investigated and various methods [20–22] have been used to construct $Cu_2O$ to enhance the electrode performance. In the study of oxide-based photoelectrodes, in addition to $Cu_2O$, the doping of elements such as $Cu^{2+}$ and $Cr^{3+}$ [23–27] is also a more popular research direction. Low-temperature hydrolysis [28], a microwave-assisted hydrothermal method [29], and sol–gel method [30–35] have been used to dope metal ions to enhance battery performance. However, these photoelectrodes are mostly used in dye-sensitized solar cells (DSSCs) and hardly used in SRFBs. In addition to the study of oxide-based photoelectrodes, photoelectrodes of some other materials have also been utilized in the field of solar flow batteries. Hu et al. [36] used III-V materials as photoelectrodes for the cells, and although a good performance was obtained, the photoelectrodes made of this material were extremely susceptible to photocorrosion, which greatly reduced the lifetime of SRFBs. Tian et al. [37] used the $MoS_2$-doped photoelectrodes which are utilized in SRFBs with good results. Its solar output energy conversion efficiency (SOEE) can reach 4.78% in 1 M electrolyte, but it is still lower at 0.17% in 0.1 M electrolyte.

Taken together as described in the above materials, in this study, $Cu_2O$ was deposited on fluorine-doped tin oxide (FTO) glass using an electrochemical deposition method at a lower cost to form FTO-$Cu_2O$ photoelectrodes, which were characterized using electrochemical methods. Finally, full-cell tests were performed using TEMPO and $VCl_3$ as redox substances. Compared to similar studies, this study differs in that the FTO-$Cu_2O$ photoelectrode was utilized in a non-aqueous SRFB. Although TEMPO and $VCl_3$ were used as the redox substances, Deep Eutectic Solvents (DESs) was used as the solvent, which can effectively inhibit the hydrogen precipitation reaction during operation, further reduce the cost of using SRFBs, and improve their performance.

## 2. Materials and Methods

### *2.1. Chemicals*

Tetrabutyl titanate ($C_{16}H_{36}O_4Ti$), acetylacetone ($CH_3COCH_2COCH_3$), absolute ethanol ($CH_3CH_2OH$), cupric chloride dihydrate ($CuCl_2{\cdot}2H_2O$) and polyethylene glycol ($HO(CH_2CH_2O)_nH$), hydrochloric acid (HCl), 2,2,6,6-tetramethylpiperidinyl-1-oxide(Tempo), choline chloride ($C_5H_{14}ClNO$), ethylene glycol ($C_2H_6O_2$), copper(II) sulfate pentahydrate

($CuSO_4 \cdot 5H_2O$), vanadium trichloride ($VCl_3$), sodium hydroxide (NaOH), DL-lactic acid ($C_3H_6O_3$), deionized water ($H_2O$), FTO glass. All chemicals were analytical grade and used without further purification.

### *2.2. Preparation of $TiO_2$ Sol*

The following steps were used to prepare the $TiO_2$ sol. First, the anhydrous ethanol and deionized water were mixed in ratio, and we used a magnetic stirrer to stir at a constant speed for 30 min to form a homogeneous solution, which was named solution A. Further, the tetrabutyl titanate solute, anhydrous ethanol solution, and acetylacetone were mixed, stirred for 30 min using a magnetic stirrer until a homogeneous solution formed, and it was named solution B. Then, concentrated hydrochloric acid (HCl) was added to a mixed solution of A and B and was stirred for 10 min in a magnetic stirrer. Polyethylene glycol was added to the mixed solution and placed in a magnetic stirrer for 30 min. The resulting mixed solution was sealed and left to age at room temperature for 24 h for use.

### *2.3. Preparation of Electrodes*

The following steps were used to prepare the photoelectrode. First, the treated $TiO_2$ sol was coated with a homogenizer FTO glass (1 cm × 1.2 cm) and the FTO glass was placed in a drying box for 10 min (70 °C) for each coat for a total of five coatings. Then, the coated FTO glass was put into a muffle furnace (400 °C) to isolate the oxygen from calcination for 1 h. Finally, we prepared photoelectrodes covered with $TiO_2$ film. The prepared photoelectrode was sealed and stored away from light.

The preparation method of FTO-$Cu_2O$ is described below. First, it was equipped with a solution containing 3 M lactic acid and 0.4 M $CuSO_4$ and named A. Then, 5 M NaOH was used to adjust the PH of solution A to 10, and this was named solution B. Next, in a three-electrode system, FTO glass (1 cm × 1.2 cm) was electrodeposited in solution B using the galvanostatic method. The current density at the time of electrodeposition was set to $-1$ mA/cm$^2$, the temperature was constant at 50 °C, and stirring occurred for 10 min using a stirrer to ensure that the stirring was uniform. The FTO-$Cu_2O$ electrode was washed with deionized water several times and dried. Finally, the electrodeposited FTO glass was calcined in a muffle furnace (350 °C) for one hour in a nitrogen environment. Figure 1 shows the preparation process for photoelectrodes.

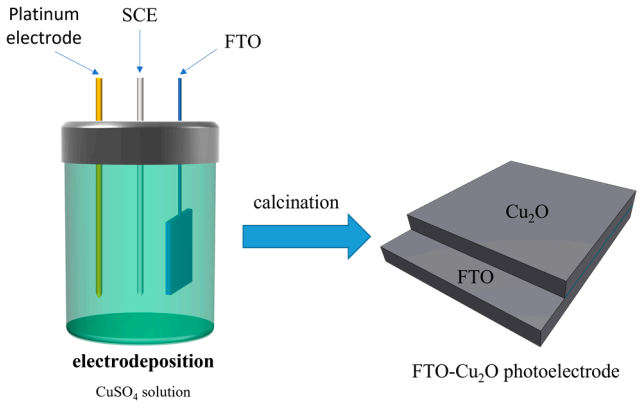


**Figure 1.** Schematic of photoelectrode preparation process.

### *2.4. Preparation of Electrolyte*

The following steps were used to prepare the electrolyte. First, choline chloride and ethylene glycol were mixed in a ratio of 1:2 to prepare a DES solution. Next, 0.1 M Tempo was dissolved into DES solution, and the positive electrolyte was obtained by stirring well. The negative electrolyte was obtained by dissolving 0.1 M $VCl_3$ solution into DES solution.

### *2.5. Photoelectrochemical Characterisation*

Photoelectrochemical studies were conducted in a three-electrode electrochemical cell using FTO-$TiO_2$ or FTO-$Cu_2O$ as a working electrode, and a saturated calomel electrode (SCE) and platinum sheet electrode as the reference and counter electrodes, respectively. In total, 0.1 M TEMPO in DES was used as the electrolyte. Linear sweep voltammetry (LSV) measurements were conducted at a scan rate of 10 $mV \cdot s^{-1}$ in the voltage range of −0.5 V to 1 V vs. SCE. The illuminated area of the working electrode was 1.0 $cm^2$. The photoelectrode was irradiated by simulated solar light using an AM 1.5 G filter. The power density of the incident light was calibrated to 100 $mW \cdot cm^{-2}$ using an optical power meter with a silicon photodetector as a certified reference.

## 3. Results

### *3.1. Half-Cell Testing*

A three-electrode system was constructed using a platinum sheet clip electrode, a platinum sheet electrode, and a SCE, and the prepared FTO-$TiO_2$ and FTO-$Cu_2O$ electrodes were tested for half-cell performance.

In order to test the photoresponsivity of the two photoelectrodes in a 0.1 M TEMPO electrolyte, a linear sweep voltammetry test was performed. The test results are shown in Figure 2. the FTO-$Cu_2O$ electrode exhibited much higher performance than the FTO-$TiO_2$ electrode, capable of achieving a photovoltage of about 430 mV vs. SCE, which is about 30 mV higher than that of the FTO-$TiO_2$ electrode. The photocurrents of the two photoelectrodes increased with the increase in the applied voltage, but the trend of the increase was more obvious for FTO-$Cu_2O$. Therefore, it can be hypothesized that the FTO-$Cu_2O$ photoelectrode produces significantly more holes per unit time than the FTO-$TiO_2$ electrode under the same electrolyte and light conditions. From this, it can be hypothesized that FTO-$Cu_2O$ deserves better battery performance, which was also reflected in the subsequent experiments.

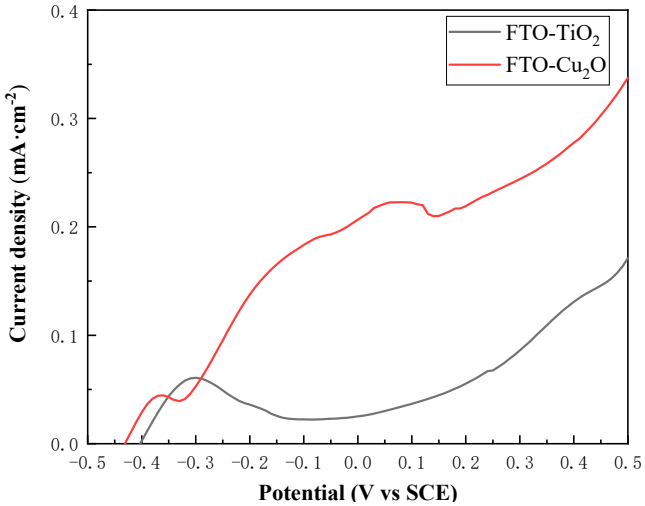


**Figure 2.** LSV in 0.1 M TEMPO with a three-electrode electrochemical system; a SCE and a Pt electrode as reference and counter electrodes, respectively.

The instantaneous current profiles of the two photoelectrodes under different bias voltages are shown in Figure 3. In the test, five different gradients of voltage were applied to the two photoelectrodes; each gradient of voltage was 0 V, 0.2 V, 0.4 V, 0.6 V, and 0.8 V. Each voltage gradient lasted for two minutes. The final experimental data were obtained as shown in Figure 3. As can be seen from the data in the figure, the FTO-$Cu_2O$ photoelectrode exhibits a superior current density compared to the FTO-$TiO_2$ photoelectrode at all five voltage gradients. This means that the FTO photoelectrode has more excellent electrical conductivity and oxidation ability due to the addition of $Cu_2O$, which may be attributed to

the higher carrier concentration of the FTO photoelectrode due to the addition of $Cu_2O$, which results in a higher performance. The change in its carrier concentration can be derived from the Mott–Schottky curve (M-S curve) in Figure 4.

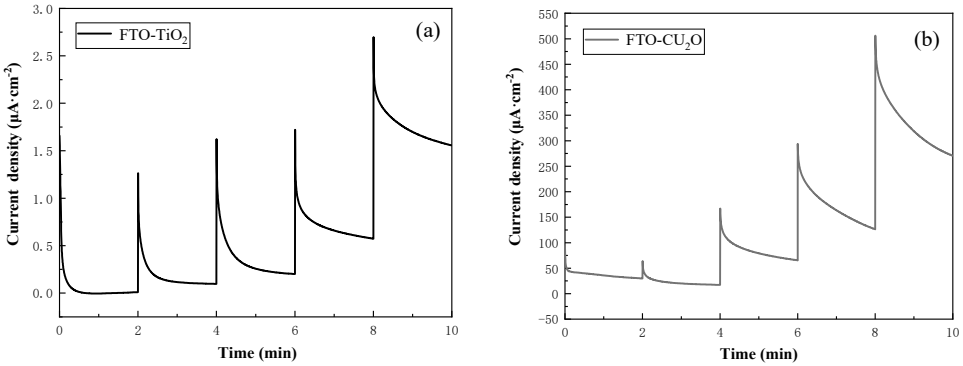


**Figure 3.** Instantaneous current plots of $TiO_2$ photoelectrodes (**a**) and $Cu_2O$ (**b**) photoelectrodes.

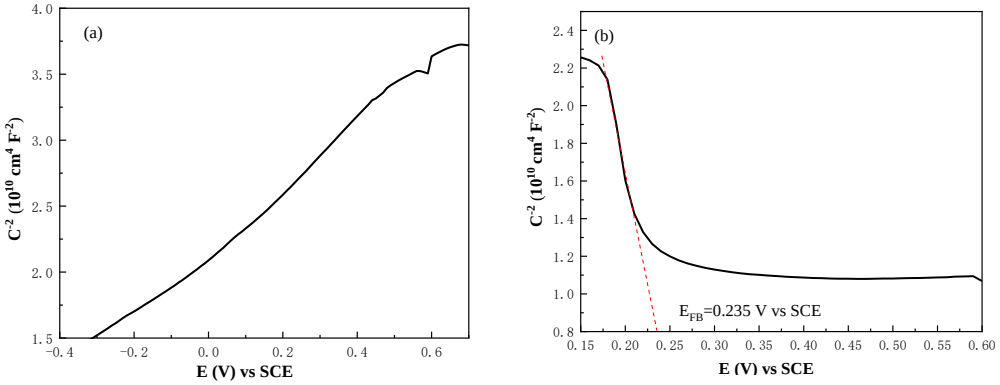


**Figure 4.** Mott–Schottky plots of FTO-$TiO_2$ electrode (**a**) and FTO-$Cu_2O$ (**b**) electrode.

The Mott–Schottky technique was applied to examine changes in the electrochemical interfaces between the electrolyte and photoelectrode. Carrier densities and flat band potentials can be accurately measured using the Mott–Schottky equation for p-type and n-type semiconductors. The Mott–Schottky formula is shown below:

$$\frac{1}{C^2} = -\frac{2}{\varepsilon\varepsilon_0 N_A A^2}\left(V - V_{fb} - \frac{k_B T}{}\right) \quad (1)$$

where $C$ is the interfacial capacitance, $\varepsilon$ is the dielectric constant of the semiconductor electrode, $\varepsilon_0$ is the vacuum permittivity ($8.854 \times 10^{-12}$ F·m$^{-1}$), e is the electron charge ($1.603 \times 10^{-19}$ C), $V_{fb}$ is the flat band potential, $N_A$ is the carrier density, $A$ is the electrode area, $V$ is the applied voltage, $k_B$ is the Boltzmann constant ($1.38 \times 10^{-23}$ J·K$^{-1}$), and $T$ is the absolute temperature. The carrier density of p-type Cuprous oxide ($N_A$) can be determined by plotting the tangent to the Mott–Schottky curve, while the flat band potential ($V_{fb}$) can be obtained from the intercept with the x-axis.

The M-S curve test results of FTO-$TiO_2$ and FTO-$Cu_2O$ electrodes are shown in Figure 4. The flat band potential $E_{fb}$ = 0.235 V vs. SCE of the FTO-$Cu_2O$ electrode can be derived from Figure 3b. The carrier concentration of the electrode can be calculated by using Equation (2), where $N_D$ is the carrier concentration, $e_0$ is the fundamental charge, $\varepsilon_{TiO_2}$ [38] is the relative dielectric constant of $TiO_2$, $\varepsilon_0$ is the dielectric constant, and $m$ is the slope of the curve. According to the data presented in Figure 3b, the $Cu_2O$ film exhibits P-type semiconductor properties with a negative slope and, therefore, the $\varepsilon$ of $Cu_2O$ is 7.6. Substituting the slope $m$ (red line) obtained from Figure 3b into the formula gives the carrier concentration of the FTO-$Cu_2O$ electrode in the TEMPO electrolyte, $N_D = 5.808 \times 10^{17}$ cm$^{-2}$. In comparison, the

carrier concentration of FTO-$TiO_2$ is $N_D = 1.5 \times 10^{17}$ $cm^{-2}$. At the same time, the flat band potentials of the FTO-$TiO_2$ and FTO-$Cu_2O$ electrodes are −0.31 V and 0.235 V, respectively. Since the flat band potential correlates with the driving force for separating electron–hole pairs in the space charge region, the flat band potential can predict the photoelectrochemical performance of the photoelectrode to some extent. For example, a shift of the flat band potential toward a positive potential indicates an improved electron transfer process as well as a reduced complexation rate of electron–hole pairs, which improves the performance of the battery. This further explains that the FTO-$Cu_2O$ electrode has a superior performance compared to the FTO-$TiO_2$ electrode in the I-t curve test. That is, the FTO-$Cu_2O$ electrode has a higher carrier concentration and a lower electron–hole pair recombination rate.

$$N_D = -\frac{2}{e_0 \varepsilon_{TiO_2} \varepsilon_0 m} \quad (2)$$

### *3.2. Full-Cell Testing*

The excellent performance of the FTO-$Cu_2O$ electrode was confirmed after half-cell testing of both photoelectrodes. In order to test its performance in a full-cell test, we tested the photo-charging performance of the FTO-$Cu_2O$ electrode using an electrochemical workstation under standard sunlight (AM 1.5 G). The test results are shown in Figure 5. The temperature of this test was controlled at 35 °C to simulate the long-term operating temperature of a one-piece solar liquid flow battery. Meanwhile, TEMPO was used as the redox substance on the photoelectrode side, and $V^{2+}$-$V^{3+}$ was used as the redox substance on the other side. The experimental results show that the average charging current density of the FTO-$Cu_2O$ electrode can reach 425.03 μA·$cm^{-2}$ under 30 min photo-charging conditions; however, the average current density of the FTO-$TiO_2$ electrode is only 116.21 μA·$cm^{-2}$. Electrochemical tests show that the photo-charging performance of the all-in-one solar liquid flow battery has been significantly improved, while the charging current did not undergo significant decay during a longer charging process. This coincides with the test results of the I-t curve and M-S curve in the previous section. That is to say, the carrier concentration of the FTO-$Cu_2O$ electrode is higher than that of the FTO-$TiO_2$ electrode under the light condition, and due to the flat band potential it possesses, it is able to obtain more open-circuit voltage and an electron driving force, which also makes its matching ability with the redox pair stronger. In addition to this, the enhancement of the photocharging performance may also be attributed to the decrease in the rate of carrier complexation during charge transfer due to the addition of $Cu_2O$.

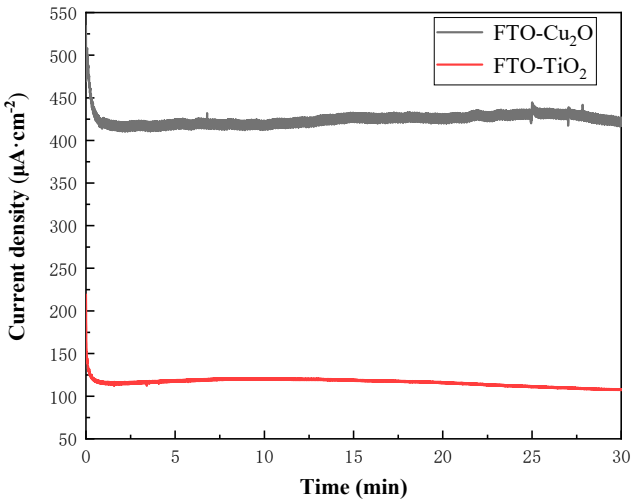


**Figure 5.** Charging current density of FTO-$Cu_2O$ photoelectrodes and FTO-$TiO_2$ photoelectrodes in the electrolyte of Tempo.

### *3.3. XRD Analysis*

In order to preliminarily analyze whether the material deposited on the surface of the FTO-$Cu_2O$ photoelectrode is $Cu_2O$ or not, we performed X-ray diffraction (XRD) of the photoelectrode, as shown in Figure 6, for the surface structure test. The $Cu_2O$ standard card (ICDD#34-1354) shows that the diffraction peaks at 2θ = 29.61°, 36.42°, 42.15°, and 72.9° correspond to the (110), (111), (200), and (311) crystal planes of $Cu_2O$. Meanwhile, the peaks appeared at 2θ = 26.23°, 33.37°, and 51.22° are the characteristic peaks of FTO glass. The results show that the electrodeposited $Cu_2O$ films are polycrystalline in structure and are predominantly (111) crystalline. Therefore, comparison of the test results in Figure 6 with the standard card confirms that the material deposited on the surface of the FTO-$Cu_2O$ photoelectrode is indeed $Cu_2O$.

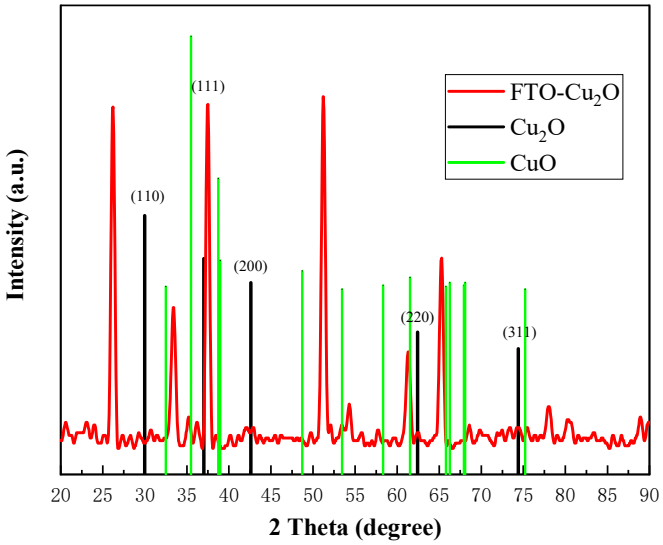


**Figure 6.** XRD pattern of $Cu_2O$ Standard card and FTO-$Cu_2O$ photoelectrode.

However, the characteristic peak of CuO appeared simultaneously at 2θ = 42°, but with a lower peak. This suggests that some of the $Cu_2O$ was oxidized to CuO during the testing process, which led to the appearance of the characteristic CuO peak. This explains the decrease in the charging current density of the battery after a long period of operation.

### *3.4. XPS Analysis*

After the above half-cell and full-cell tests, the FTO-$Cu_2O$ photoelectrode has a higher photocharging performance than the common $TiO_2$ electrode. In order to confirm the successful deposition of $Cu_2O$ on the surface of the FTO electrode and to prove that the improved full-cell performance is caused by the presence of $Cu_2O$, we performed X-ray photoelectron spectroscopy (XPS) analysis on the FTO-$Cu_2O$ photoelectrode. The results of the XPS test of the FTO-$Cu_2O$ photoelectrode are shown in Figure 7. The yellow and blue lines in Figure 7 represent the XPS baselines of each corresponding element, respectively.

We corrected the peaks obtained (BE) for each element with the exotic carbon 1s peak (BE 284.8 eV) and fitted them using a hybrid Gauss–Lorentz curve. As shown in Figure 7b, our fitting of the Cu 2p dual peaks reveals that the binding energies of the $Cu_2O$ film in the deposited state in the FTO-$Cu_2O$ photoelectrode are 932.7 eV and 953.1 eV, which correspond to the binding energy states of Cu $2p_{3/2}$ and Cu $2p_{1/2}$, respectively. Therefore, it can be concluded that the bimodal peaks of the binding energy of Cu 2p on the FTO-$Cu_2O$ photoelectrode correspond to metal Cu and $Cu^+$, respectively.

Figure 7c shows the XPS test curve of O 1s, whose binding energy peak at 532.2 eV corresponds to the Ti-O bond in $TiO_2$.

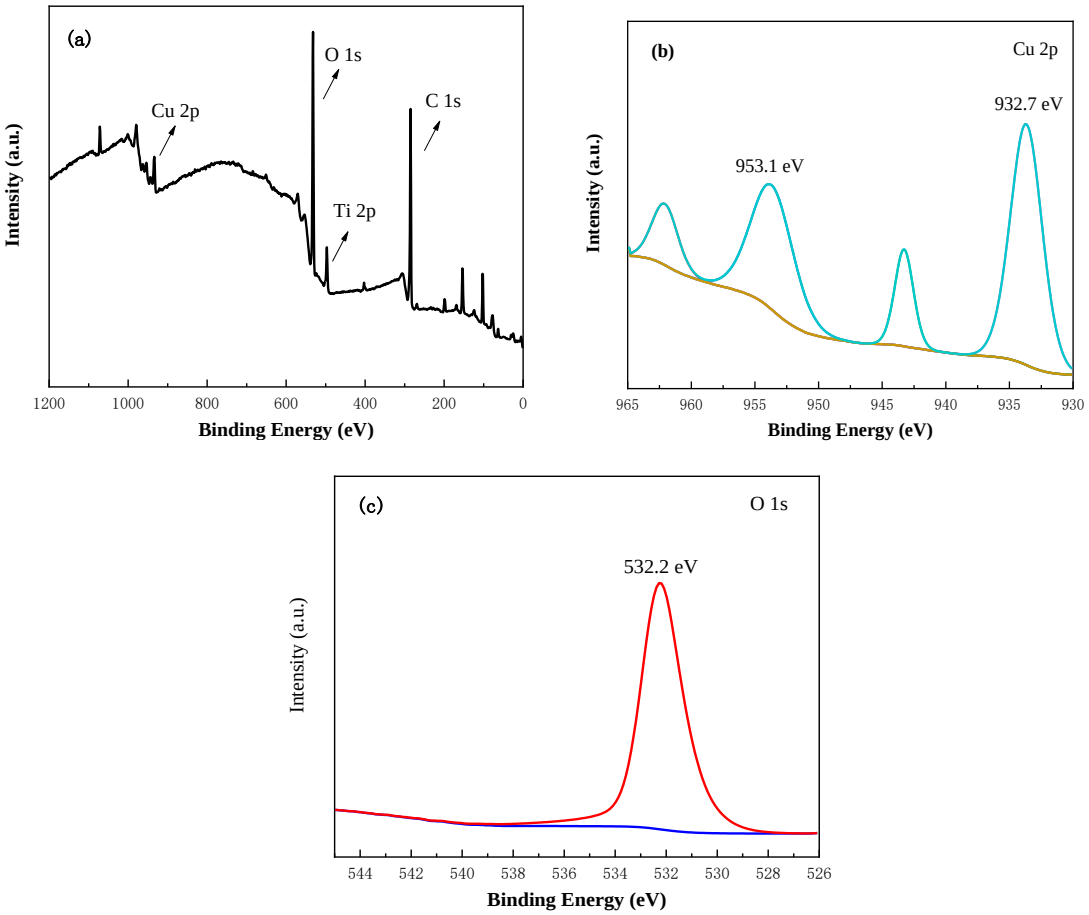


**Figure 7.** XPS full-spectrum analysis of the samples of $Cu_2O$-$TiO_2$ photoelectrode (**a**); high−resolution XPS profile of Cu 2p and O 1s of $Cu_2O$-$TiO_2$ photoelectrode sample (**b**,**c**).

### *3.5. UV-Vis Analysis*

Figure 8 shows the visible light absorption recorded on the surface of FTO-$TiO_2$ and FTO-$Cu_2O$ electrodes using ultraviolet–visible spectroscopy (UV-vis). The spectral resolution is 1 nm, and the FTO glass was used as a blank sample. The dotted line in the figure represents the tangential projection of plasma polaritons with absorbance value = 0. As can be seen in Figure 8, the FTO-$TiO_2$ photoelectrode can only absorb UV light below 350 nm; however, the addition of the $Cu_2O$ heterojunction allows the photoelectrode to extend the absorption wavelength to about 400 nm, and even a small amount of absorption in the visible wavelength band. After tangentially processing the UV spectral data of the two electrodes, Equation (3) can be used to approximate the band gap of the photoelectrode to further explain the excellent performance of the FTO-$Cu_2O$ electrode.

$$E = \frac{hc}{\lambda} \tag{3}$$

where $E$ corresponds to the absorbed energy, $h$ is the Plank's constant ($6.626 \times 10^{-36}$ J·s), $c$ is the speed of light ($3.8 \times 10^{8}$ m·s$^{-1}$), and $\lambda$ corresponds to the wavelength, expressed in meters. The band gap of the FTO-$TiO_2$ photoelectrode is calculated to be about 3.54 eV; however, the band gap of the FTO-$Cu_2O$ photoelectrode is about 2.9 eV. It can be seen that the addition of $Cu_2O$ reduces the band gap of $TiO_2$, thereby reducing the difficulty of electron transition. Furthermore, the FTO-$Cu_2O$ photoelectrode with a heterojunction structure absorbs wave sunlight not only in the ultraviolet band but also has a certain absorption and utilization capacity in the visible light band. This is consistent with the results obtained in the UV-vis diagram.

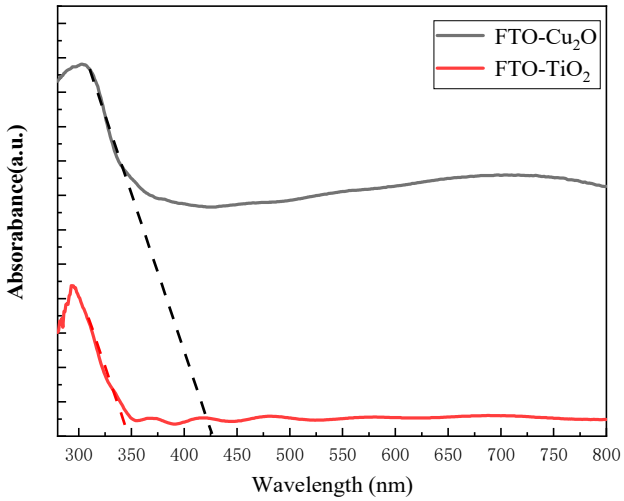


**Figure 8.** UV-vis of FTO-$TiO_2$ photoelectrode and FTO-$Cu_2O$ photoelectrode.

However, although the solar light utilization range of the FTO-$Cu_2O$ photoelectrode was extended to 400 nm under the effect of the $Cu_2O$ heterojunction structure, there is still a gap with the performance of the $Cu_2O/TiO_2$/FTO photoelectrode obtained in the study of Felipe et al. [19], where the solar light absorption range of the photoelectrode could be extended up to 500 nm. This is due to the fact that the $Cu_2O$ electrodeposited on the surface has poor stability and will be oxidized to CuO rapidly during use, thus reducing the performance of the electrode, which can be seen in the previous XRD test. Therefore, how to improve the stability of $Cu_2O$ has become a focus and difficulty in the subsequent research.

## 4. Conclusions

In this study, $Cu_2O$ was successfully deposited on the surface of FTO glass using an electrochemical deposition method, and the prepared photoelectrode was used in a one-piece solar liquid flow battery. The LSV, instantaneous current plots, and Mott–Schottky test results show that the FTO-$Cu_2O$ photoelectrode possesses P-type semiconductor characteristics. At the same time, the FTO-$Cu_2O$ photoelectrode possesses a more positive flat band potential compared to FTO-$TiO_2$, which allows it to obtain more holes under the light condition, thus increasing its carrier concentration. In addition, $TiO_2$, as an n-type semiconductor, forms a heterostructure type with $Cu_2O$, which reduces the electron–hole pair recombination rate of the photoelectrode and further improves the cell performance. The UV-vis test results showed that the FTO-$Cu_2O$ photoelectrode has a wider absorption range and stronger absorption ability for sunlight in the UV range. The full-cell test results showed that the photo-charging current density of FTO-$Cu_2O$ can reach 425.03 $\mu A \cdot cm^{-2}$ under an unbiased condition, which is 365.74% higher compared with that of the FTO-$TiO_2$ electrode. Moreover, it can be stabilized at a high current density for a longer time. However, although the electrode can be stabilized for longer, the charging current density of the battery still gradually decreases as the operating time continues to increase, and the SOC value of the battery at this time is far from reaching 100%, which is presumed to be caused by the poor stability of the $Cu_2O$ on the electrode surface, and part of the $Cu_2O$ is oxidized to CuO. This conclusion can be confirmed in the XRD and XPS tests. Overall, this study provides a low-cost option for the selection of photoelectrodes for non-aqueous integrated solar redox flow batteries.

**Author Contributions:** Conceptualization, H.S. and Z.G. (Zhizhong Guo); Methodology, Z.Z.; validation, P.L.; resources, Z.G. (Zixing Gu); software, Q.M.; writing—original draft preparation, Z.Z.; writing—review and editing, Q.X. All authors have read and agreed to the published version of the manuscript.

**Funding:** NSFC: China (No. 52276066, No. 51676092); Six-Talent-Peaks Project in Jiangsu Province (No. 2016-XNY-015); High-Tech Research Key Laboratory of Zhenjiang City (No. SS2018002); Hainan Natural Science Foundation (No. 521RC740).

**Data Availability Statement:** Not applicable.

**Acknowledgments:** The work described in this paper was fully supported by the grants from the NSFC, China (No. 52276066, No. 51676092), the Six-Talent-Peaks Project in Jiangsu Province (No. 2016-XNY-015), the High-Tech Research Key Laboratory of Zhenjiang City (No. SS2018002), and Hainan Natural Science Foundation (No. 521RC740).

**Conflicts of Interest:** The authors declare no conflict of interest.

## References

1. Cui, H.; Zhao, W.; Yang, C.; Yin, H.; Lin, T.; Shan, Y.; Xie, Y.; Gu, H.; Huang, F. Black $TiO_2$ nanotube arrays for high-efficiency photoelectrochemical water-splitting. *J. Mater. Chem. A* **2014**, *2*, 8612–8616. [CrossRef]
2. Fujishima, A.; Rao, T.N.; Tryk, D.A. Titanium dioxide photocatalysis. *J. Photochem. Photobiol. C Photochem. Rev.* **2000**, *1*, 1–21. [CrossRef]
3. Ohno, T.; Mitsui, T.; Matsumura, M. Photocatalytic Activity of S-doped $TiO_2$ Photocatalyst under Visible Light. *Chem. Lett.* **2003**, *32*, 364–365. [CrossRef]
4. Akpan, U.G.; Hameed, B.H. The advancements in sol–gel method of doped-$TiO_2$ photocatalysts. *Appl. Catal. A Gen.* **2010**, *375*, 1–11. [CrossRef]
5. Nakata, K.; Fujishima, A. $TiO_2$ photocatalysis: Design and applications. *J. Photochem. Photobiol. C Photochem. Rev.* **2012**, *13*, 169–189. [CrossRef]
6. Fujishima, A.; Honda, K. Electrochemical Photolysis of Water at a Semiconductor Electrode. *Nature* **1972**, *238*, 37–38. [CrossRef]
7. Butburee, T.; Bai, Y.; Wang, H.; Chen, H.; Wang, Z.; Liu, G.; Zou, J.; Khemthong, P.; Lu, G.Q.M.; Wang, L. 2D Porous $TiO_2$ Single-Crystalline Nanostructure Demonstrating High Photo-Electrochemical Water Splitting Performance. *Adv. Mater.* **2018**, *30*, 1705666. [CrossRef]
8. Whitley, S.; Bae, D. Perspective-Insights into Solar-Rechargeable Redox Flow Cell Design: A Practical Perspective for Lab-Scale Experiments. *J. Electrochem. Soc.* **2021**, *168*, 120517. [CrossRef]
9. Cao, L.Y.; Skyllas-Kazacos, M.; Wang, D.W. Solar Redox Flow Batteries: Mechanism, Design, and Measurement. *Adv. Sustain. Syst.* **2018**, *2*, 1800031. [CrossRef]
10. Li, W.J.; Jin, S. Design Principles and Developments of Integrated Solar Flow Batteries. *Acc. Chem. Res.* **2020**, *53*, 2611–2621. [CrossRef]
11. Binetti, E.; El Koura, Z.; Bazzanella, N.; Carotenuto, G.; Miotello, A. Synthesis of mesoporous ITO/$TiO_2$ electrodes for optoelectronics. *Mater. Lett.* **2015**, *139*, 355–358. [CrossRef]
12. Sivula, K.; van de Krol, R. Semiconducting materials for photoelectrochemical energy conversion. *Nat. Rev. Mater.* **2016**, *1*, 15010. [CrossRef]
13. Yang, W.; Moon, J. Recent Advances in Earth-Abundant Photocathodes for Photoelectrochemical Water Splitting. *ChemSusChem* **2019**, *12*, 1889–1899. [CrossRef]
14. Yang, Y.; Niu, S.; Han, D.; Liu, T.; Wang, G.; Li, Y. Progress in Developing Metal Oxide Nanomaterials for Photoelectrochemical Water Splitting. *Adv. Energy Mater.* **2017**, *7*, 1700555. [CrossRef]
15. Ciria-Ramos, I.; Juarez-Perez, E.J.; Haro, M. Solar Energy Storage Using a $Cu_2O$-$TiO_2$ Photocathode in a Lithium Battery. *Small* **2023**, *19*, 2301244. [CrossRef] [PubMed]
16. Yin, T.-H.; Liu, B.-J.; Lin, Y.-W.; Li, Y.-S.; Lai, C.-W.; Lan, Y.-P.; Choi, C.; Chang, H.-C.; Choi, Y. Electrodeposition of Copper Oxides as Cost-Effective Heterojunction Photoelectrode Materials for Solar Water Splitting. *Coatings* **2022**, *12*, 1839. [CrossRef]
17. El Koura, Z.; Cazzanelli, M.; Bazzanella, N.; Patel, N.; Fernandes, R.; Arnaoutakis, G.E.; Gakamsky, A.; Dick, A.; Quaranta, A.; Miotello, A. Synthesis and Characterization of Cu and N Codoped RF-Sputtered $TiO_2$ Films: Photoluminescence Dynamics of Charge Carriers Relevant for Water Splitting. *J. Phys. Chem. C* **2016**, *120*, 12042–12050. [CrossRef]
18. Tilley, S.D. Recent Advances and Emerging Trends in Photo-Electrochemical Solar Energy Conversion. *Adv. Energy Mater.* **2019**, *9*, 1802877. [CrossRef]
19. Matamala-Troncoso, F.; Sáez-Navarrete, C.; Mejía-López, J.; García, G.; Rebolledo-Oyarce, J.; Nguyen, C.K.; MacFarlane, D.R.; Isaacs, M. Experimental and theoretical study of synthesis and properties of $Cu_2O/TiO_2$ heterojunction for photoelectrochemical purposes. *Surf. Interfaces* **2023**, *37*, 102751. [CrossRef]
20. Huang, L.; Zhang, S.; Peng, F.; Wang, H.; Yu, H.; Yang, J.; Zhang, S.; Zhao, H. Electrodeposition preparation of octahedral-$Cu_2O$-loaded $TiO_2$ nanotube arrays for visible light-driven photocatalysis. *Scr. Mater.* **2010**, *63*, 159–161. [CrossRef]
21. Marathey, P.; Patel, B.; Khanna, S.; Vanpariya, A.; Ray, A. Photoelectrochemical characteristics of electrodeposited cuprous oxide with protective over layers for hydrogen evolution reactions. *Int. J. Hydrogen Energy* **2021**, *46*, 16431–16439. [CrossRef]

22. Rubino, A.; Zanoni, R.; Schiavi, P.G.; Latini, A.; Pagnanelli, F. Two-Dimensional Restructuring of $Cu_2O$ Can Improve the Performance of Nanosized n-$TiO_2$/p-$Cu_2O$ Photoelectrodes under UV-Visible Light. *Acs Appl. Mater. Interfaces* **2021**, *13*, 47932–47944. [CrossRef] [PubMed]
23. Asemi, M.; Maleki, S.; Ghanaatshoar, M. Cr-doped $TiO_2$-based dye-sensitized solar cells with Cr-doped $TiO_2$ blocking layer. *J. Sol-Gel Sci. Technol.* **2017**, *81*, 645–651. [CrossRef]
24. Gayathri, V.; John Peter, I.; Rajamanickam, N.; Ramachandran, K. Improved performance of dye-sensitized solar cells by Cr doped $TiO_2$ nanoparticles. *Mater. Today Proc.* **2021**, *35*, 23–26. [CrossRef]
25. Kim, C.; Kim, K.S.; Kim, H.Y.; Han, Y.S. Modification of a $TiO_2$ photoanode by using Cr-doped $TiO_2$ with an influence on the photovoltaic efficiency of a dye-sensitized solar cell. *J. Mater. Chem.* **2008**, *18*, 5809–5814. [CrossRef]
26. Nguyen, H.H.; Gyawali, G.; Hoon, J.S.; Sekino, T.; Lee, S.W. Cr-doped $TiO_2$ nanotubes with a double-layer model: An effective way to improve the efficiency of dye-sensitized solar cells. *Appl. Surf. Sci.* **2018**, *458*, 523–528. [CrossRef]
27. Xie, Y.; Huang, N.; You, S.; Liu, Y.; Sebo, B.; Liang, L.; Fang, X.; Liu, W.; Guo, S.; Zhao, X.-Z. Improved performance of dye-sensitized solar cells by trace amount Cr-doped $TiO_2$ photoelectrodes. *J. Power Sources* **2013**, *224*, 168–173. [CrossRef]
28. Chahid, S.; de los Santos, D.M.; Alcantara, R. The effect of Cu-doped $TiO_2$ photoanode on photovoltaic performance of dye-sensitized solar cells. In Proceedings of the 3rd International Conference on Smart City Applications (SCA'), Tetouan, Morocco, 10–11 October 2018.
29. Ünlü, B.; Özacar, M. Effect of Cu and Mn amounts doped to $TiO_2$ on the performance of DSSCs. *Sol. Energy* **2020**, *196*, 448–456. [CrossRef]
30. Dhonde, M.; Sahu, K.; Murty, V.V.S.; Nemala, S.S.; Bhargava, P. Surface plasmon resonance effect of Cu nanoparticles in a dye sensitized solar cell. *Electrochim. Acta* **2017**, *249*, 89–95. [CrossRef]
31. Javed, H.M.A.; Sarfaraz, M.; Mustafa, M.S.; Que, W.X.; Ateeq ur, R.; Awais, M.; Hussain, S.; Qureshi, A.A.; Iqbal, M.Z.; Khan, M.A. Efficient Cu/rGO/$TiO_2$ nanocomposite-based photoanode for highly-optimized plasmonic dye-sensitized solar cells. *Appl. Nanosci.* **2020**, *10*, 2419–2427. [CrossRef]
32. Khan, M.I.; Rehman, M.A.; Saleem, M.; Baig, M.R.; Rehman, S.; Farooq, W.A.; Atif, M.; Hanif, A. Synthesis and characterization of nanostructured photoanodes for dye sensitized solar cells. *Ceram. Int.* **2019**, *45*, 20589–20592. [CrossRef]
33. Park, J.-Y.; Kim, C.-S.; Okuyama, K.; Lee, H.-M.; Jang, H.-D.; Lee, S.-E.; Kim, T.-O. Copper and nitrogen doping on $TiO_2$ photoelectrodes and their functions in dye-sensitized solar cells. *J. Power Sources* **2016**, *306*, 764–771. [CrossRef]
34. Venumbaka, M.R.; Akkala, N.; Duraisamy, S.; Sigamani, S.; Poola, P.K.; D, S.R.; Marepally, B.C. Performance of $TiO_2$, Cu-$TiO_2$, and N-$TiO_2$ nanoparticles sensitization with natural dyes for dye sensitized solar cells. *Mater. Today Proc.* **2022**, *49*, 2747–2751. [CrossRef]
35. Zatirostami, A. A dramatic improvement in the efficiency of $TiO_2$-based DSSCs by simultaneous incorporation of Cu and Se into its lattice. *Opt. Mater.* **2021**, *117*, 111110. [CrossRef]
36. Hu, S.; Shaner, M.R.; Beardslee, J.A.; Lichterman, M.; Brunschwig, B.S.; Lewis, N.S. Amorphous $TiO_2$ coatings stabilize Si, GaAs, and GaP photoanodes for efficient water oxidation. *Science* **2014**, *344*, 1005–1009. [CrossRef] [PubMed]
37. Tian, G.; Jervis, R.; Briscoe, J.; Titirici, M.; Jorge Sobrido, A. Efficient harvesting and storage of solar energy of an all-vanadium solar redox flow battery with a MoS2@$TiO_2$ photoelectrode. *J. Mater. Chem. A* **2022**, *10*, 10484–10492. [CrossRef]
38. Hossain, M.A.; Al-Gaashani, R.; Hamoudi, H.; Al Marri, M.J.; Hussein, I.A.; Belaidi, A.; Merzougui, B.A.; Alharbi, F.H.; Tabet, N. Controlled growth of Cu2O thin films by electrodeposition approach. *Mater. Sci. Semicond. Process.* **2017**, *63*, 203–211. [CrossRef]